NANO LETTERS

Letter

pubs.acs.org/NanoLett

Hot Electron Transistor with van der Waals Base-Collector Heterojunction and High-Performance GaN Emitter

Ahmad Zubair,*[,†] Amirhasan Nourbakhsh,[†] Jin-Yong Hong,[†] Meng Qi,[‡] Yi Song,[†] Debdeep Jena,[§] Jing Kong,[†] Mildred Dresselhaus,[†,∥] and Tomás Palacios[†]

[†]Department of Electrical Engineering Computer Science, Massachusetts Institute of Technology, 77 Massachusetts Avenue, Cambridge, Massachusetts 02139, United States

[‡]Electrical Engineering Department, University of Notre Dame, Notre Dame, Indiana 46556, United States

[§]School of Electrical and Computer Engineering, Cornell University, Ithaca, New York 14850, United States

[∥]Department of Physics, Massachusetts Institute of Technology, 77 Massachusetts Avenue, Cambridge, Massachusetts 02139, United States

Supporting Information

ABSTRACT: Single layer graphene is an ideal material for the base layer of hot electron transistors (HETs) for potential terahertz (THz) applications. The ultrathin body and exceptionally long mean free path maximizes the probability for ballistic transport across the base of the HET. We demonstrate for the first time the operation of a high-performance HET using a graphene/WSe_2 van der Waals (vdW) heterostructure as a base-collector barrier. The resulting device with a GaN/AlN heterojunction as emitter, exhibits a current density of 50 A/cm^2, direct current gain above 3 and 75% injection efficiency, which are record values among graphene-base HETs. These results not only provide a scheme to overcome the limitations of graphene-base HETs toward THz operation but are also the first demonstration of a GaN/vdW heterostructure in HETs, revealing the potential for novel electronic and optoelectronic applications.

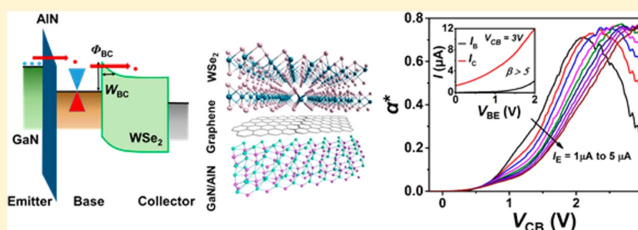

KEYWORDS: *Hot electron transistor, graphene, GaN, WSe_2, van der Waals heterostructure, tunneling, transition metal dichalcogenides*

The hot electron transistor[1] is a promising device concept that could be used to overcome the limitations of heterojunction bipolar transistors (HBTs) and high electron mobility transistors (HEMTs) in ultrahigh frequency applications. The HET is a unipolar and majority carrier device where the base-to-emitter voltage controls the transport of ballistic hot electrons through a transit layer smaller than the mean free path (λ_{mfp}) of the carriers. Hence, HETs have the potential to exhibit a superior high-frequency performance relative to HBTs (limited by the diffusion of the minority carriers across the base) and HEMTs (limited by the saturation velocity of carriers and the lithography of the gate).[1] As shown schematically in Figure 1a, a typical HET structure consists of a hot electron injector (emitter/emitter-barrier stack), a transport layer (base) and a hot electron analyzer or filter (collector-barrier/collector-stack). The HET can be considered as a combination of two back-to-back diodes connected in series, namely the E-B diode and the B-C diode. Under the operating conditions, the emitter-base (E-B) diode is forward biased ($V_{BE} > 0$ V) and electrons are injected into the base with an excess energy above the Fermi energy of the base ($eV_{BE}-E_f$). If the base-collector (B-C) diode is then reverse biased ($V_{CB} > 0$ V), it will allow the hot electrons reaching the base to travel to the collector with minimal scattering (quasi-ballistically) (Figure 1a). However, if $V_{CB} < 0$ V, the energy barrier for the base electrons (shown by the dotted lines in Figure 1a) will increase and majority of the injected electrons will thermalize in the base by scattering and quantum mechanical reflection and eventually contribute to the base leakage current. Several material systems have been used for HET development including metal thin films,[1,2] nonpolar III−V semiconductor heterostructures,[3−6] complex oxides,[7] and superconducting materials.[8] However, the successful demonstration of high-performance HETs have been limited by the technological inability to scale the base thickness below the λ_{mfp} of the carriers and electrostatic decoupling of the collector from emitter. In the thick base regions used so far, the injected hot electrons are thermalized in the base as a result of inelastic (intra- and intervalley[6] electron−electron, electron−phonon) and elastic (impurities) scattering. To reduce intervalley scattering, wide bandgap materials such as GaN have been recently used,[9,10] as they show large intervalley separation. These GaN-based devices have demonstrated excellent current

Received: February 2, 2017
Revised: April 16, 2017
Published: April 17, 2017

ACS Publications © 2017 American Chemical Society

DOI: 10.1021/acs.nanolett.7b00451
Nano Lett. 2017, 17, 3089−3096

Downloaded via CORNELL UNIV on August 17, 2018 at 04:29:19 (UTC).
See https://pubs.acs.org/sharingguidelines for options on how to legitimately share published articles.

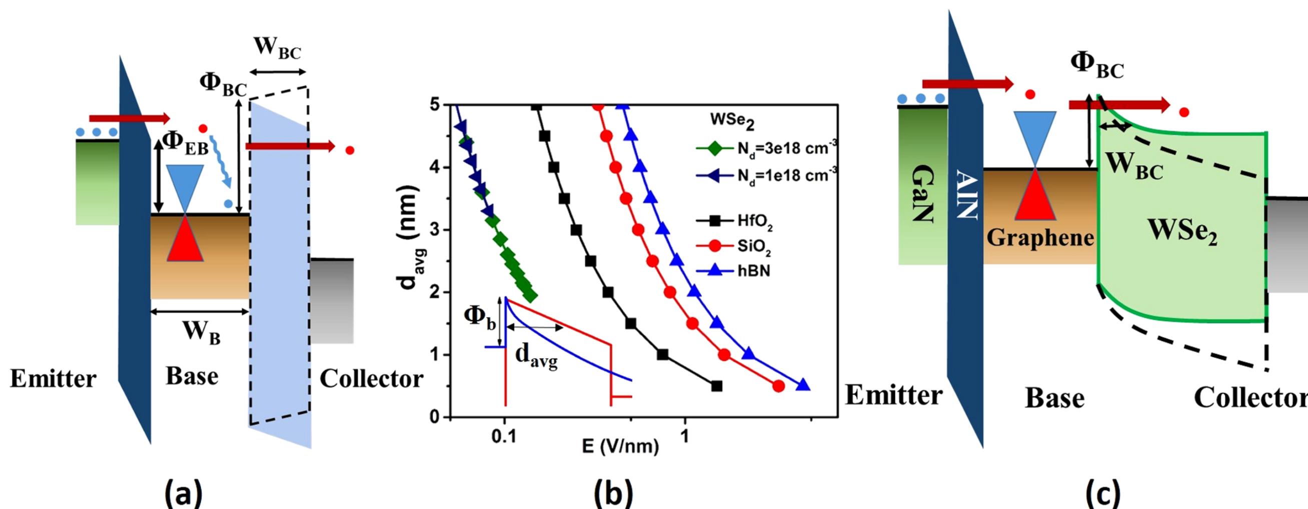

Figure 1. (a) Schematic energy band diagram of a GHET with an insulator-collector barrier along the vertical direction in the on-state for $V_{CB} > 0$ V (solid line) and $V_{CB} < 0$ V (dotted line), showing the carrier flow direction and relevant design parameters. (b) Average base-collector tunneling barrier width for electrons injected in graphene from the emitter as a function of electric field for different base-collector barrier materials. (c) Energy band diagram of the proposed GHET with a graphene/semiconductor Schottky barrier in the on-state for $V_{CB} > 0$ V (dotted line) and $V_{CB} < 0$ V (solid line).

gain (>10)[11] and current density (~kA/cm^2)[11,12] at room temperature; however, similar to other bulk three-dimensional semiconductors the growth of an ultrascaled base layer still remains a challenge.

Single atomic layer two-dimensional (2D) materials are naturally suitable for applications requiring ultrathin, defect-free films. Several vertical tunneling devices[13] for both logic (tunneling transistors,[14] barristors[15]) and high-frequency applications (resonant tunneling device[16]) have been demonstrated using these materials. Monolayer graphene with ultrahigh mobility and a dangling-bond-free inert surface is an ideal candidate as a low resistance, scattering-free base material in HETs that can overcome the growth-related limitations in bulk semiconductors. Theoretical studies have predicted that with an optimized structure, a maximum unity gain operating frequency (f_T) up to several terahertz (THz),[17−21] I_{on}/I_{off} over 10^5, and high current gain[19,22,23] can be achieved in graphene-base HETs (GHET). The initial experimental demonstrators of GHETs[24−27] showed successful operation in terms of current modulation (on−off ratio >10^5) but suffered from low output current density (~μA/cm^2), low current gain, low injection efficiency, low output impedance and high threshold voltage. These limitations are not intrinsic to the use of graphene as a base material and can be overcome by a careful design and optimization of the device, which are the goals of the present work.

One of the major shortcomings of the GHETs reported so far is the low output current density, which can be increased by improving the (i) emitter current (I_E) and (ii) injection efficiency or base transport factor, defined by

$$\alpha = \frac{I_C}{I_E}$$

as shown in the band diagram in Figure 1a, the quantity I_E is dominated by the quantum mechanical tunneling of electrons from the emitter to the base. According to the WKB approximation, the tunneling probability (T) through a barrier can be defined as

$$T \propto e^{-\gamma}$$

where γ is a function of both the barrier thickness and height. Hence, the emitter current can be significantly increased by scaling the barrier thickness.[27] However, the initial graphene HETs suffer from a low injection current density from the emitter through the emitter-base barrier due to the thick oxide layers (>5 nm SiO_2) typically used as the emitter-base barrier.[24,25] Narrower tunneling barriers would improve the tunneling probability and also allow a lower turn-on voltage, which would allow the low voltage operation of the device, currently absent in existing HETs (with $V_{BE} > 2$ V). In the devices reported in this Letter (Figure 2a), we use ultrathin AlN on GaN as the emitter stack. The use of all-binary heterostructures eliminates leakage current due to percolation transport arising from random alloy fluctuation,[28] while the large polarization difference between GaN and AlN enables a very high 2-DEG density in the GaN-side of the heterostructure, which allows for low emitter resistance. Moreover, GaN/AlN heterostructure has higher tunneling current than Si/SiO_2 due to smaller conduction band offset at the junction. The epitaxial nature of the AlN/GaN also provides high quality trap-free interface.

To improve the output current density, the common-base injection efficiency, α, should be close to unity. α can be expressed as

$$\alpha = \alpha_B \alpha_{BC} \alpha_C$$

where α_B, α_{BC}, and α_C represents base efficiency, base-collector barrier filtering efficiency and collector efficiency, respectively. The base efficiency is defined as

$$\alpha_B = \exp\left(-\frac{W_B}{\lambda_{mfp}}\right)$$

where W_B is the physical thickness of the base and λ_{mfp} is the carrier mean free path. Monolayer graphene has near unity α_B because of its atomically thin nature (t = 3.4 Å), which is superior to any other bulk material. In the case of GaN, the mean free path is around 15 nm[29] and α_B will be fundamentally

DOI: 10.1021/acs.nanolett.7b00451
Nano Lett. 2017, 17, 3089−3096

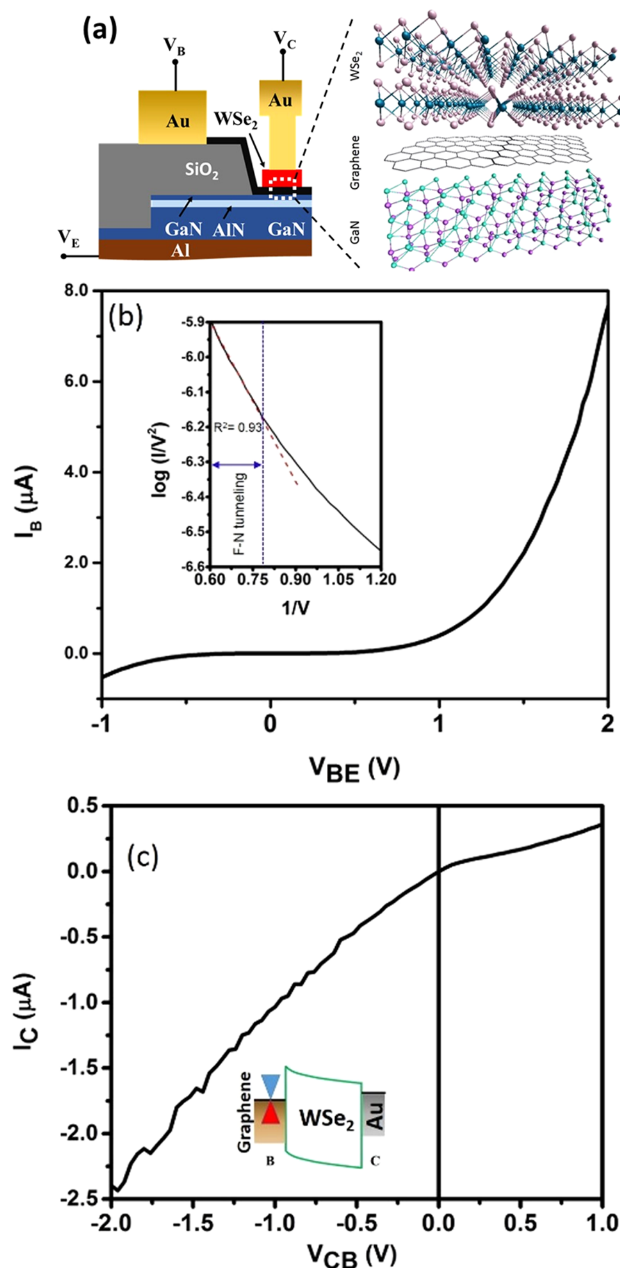

Figure 2. (a) Schematic cross-section of the fabricated GHET with key terminal voltages. $I-V$ characteristics of the (b) emitter-base (GaN/AlN/graphene) and (c) base-collector (graphene/WSe_2/Au) heterojunction diode. Fowler-Nordheim fitting (red dashed line) of the diode $I-V$ characteristics for the B-E diode is shown in the inset.

limited even in the ultrascaled base. However, the relatively low values of α in GHETs arise from the poor filtering efficiency (α_{BC}), which will be systematically studied below.

The filtering efficiency depends on both the quantum mechanical reflection at the barrier and tunneling conductance of the barrier. To minimize the reflection, base-collector band-offset (Φ_{BC}) should be smaller than the emitter-base band-offset (Φ_{EB}) (Figure 1a), but if Φ_{BC} is too low then cold electron leakage from the base to the collector will be higher, which will degrade the ballistic injection efficiency.

Moreover, to efficiently tune the barrier width with an applied bias and thus modulate the tunneling probability, the barrier shape needs to be triangular rather than trapezoidal[27] as for a trapezoidal barrier, the effective barrier thickness is equal to its physical thickness. Figure 1b shows a comparison of the average tunnel barrier width (computed at the full width at half-maximum (fwhm) of the tunnel barrier width) for different conventional dielectrics at the minimum electric field required to change the barrier to a triangular shape from trapezoidal. Owing to the large conduction band offset with graphene (that is 4.5 eV for hBN), the required electric field to achieve a particular tunnel barrier width is relatively large so the device needs to be operated at a relatively large V_{BC}, which makes it prone to breakdown. Therefore, to improve α_{BC}, the base-collector dielectric barrier has to be ultrathin. Moreover, the base-collector junction in these devices cannot completely screen the emitter electric field that causes severe increase in output conductance. Apart from this fact, forming ultrathin layers of the dielectrics on a graphene base is very challenging because the chemically inert, hydrophobic surface of graphene does not allow conformal nucleation of atomic layer deposition (ALD) thin film oxides.[30] Therefore, as a result, relatively thick layers of oxides (∼15−55 nm)[24,25,27,31] have been used so far to achieve conformal, pinhole free barriers. Beside their thickness, these dielectrics have relatively large conduction band offsets with graphene (3.3 eV for Al_2O_3 and 2 eV for HfO_2), which cause a dramatic decrease of the current tunneling probability through the barrier and, thus, α_{BC} becomes very poor. Alternatively, one can use a semiconductor instead of an oxide dielectric as the base-collector barrier. Because the semiconductors can typically form a smaller band offset with graphene compared to oxides (for example, ∼0.3 eV for n-Si[15], ∼0.5 eV for Ge, ∼0.7 eV for GaN[32]), they have a strong band bending effect at the Schottky junction with a metal, which can provide a steep triangular barrier. Therefore, the required field to achieve a given tunnel barrier width is much lower than for insulators (Figure 1b). The doping density and the barrier thickness are additional parameters that can be tuned in semiconductor-based barriers to further improve α_{BC}. Figure 1c shows the energy band diagram of the proposed HET structure with the graphene/semiconductor heterojunction as the base-collector barrier. The effective tunnel barrier width (W_{BC}) at nonpositive V_{CB} (solid line) is large enough to block the tunneling of carriers from the base to collector, similar to a conventional metal/semiconductor heterojunction. In the reverse bias condition ($V_{BC} > 0$ V), the tunnel barrier width is reduced (dotted lines), therefore the carrier tunneling probability would increase.

However, the deposition of conventional semiconductors on graphene encounters the same challenges as the oxides, that is, nonuniformity and poor material quality. In this work, we overcame this difficulty by using layered semiconductors from the family of transition metal dichalcogenides (WSe_2, MoS_2, SnS_2, and so forth). Thin-films of these materials, as thin as a monolayer, can be easily obtained by mechanical exfoliation owing to weak interlayer van der Waals forces. The atomic layers can then be mechanically transferred on any arbitrary substrate or paired with another atomic layer to form a van der Waals heterojunction with a defect-free, sharp interface. Herein, we propose to use a graphene/WSe_2 base-collector junction (Figure 2a), where the graphene-base forms a Schottky barrier to the WSe_2 layer. WSe_2 is an ambipolar semiconductor with a bulk bandgap of 1.2 eV that increases to 1.6 eV in the monolayer. This configuration would potentially benefit from the small graphene/WSe_2 band offset energy (∼0.54 eV[33]), which is in the typical range for a graphene/semiconductor

DOI: 10.1021/acs.nanolett.7b00451
Nano Lett. 2017, 17, 3089−3096

junction. The layered nature of WSe_2 enables a thickness control from the monolayer ($t \sim 0.65$ nm) to bulk. In this work, we also study the effect of collector layer thickness on the performance metrics of GHET.

Figure 2a presents the schematic of the device structure used in this work. We have used a bulk n-GaN ($N_d \sim 10^{19}$ cm^{-3}) substrate grown by the ammonothermal method to achieve a low threading dislocation defect (TDD) density ($<10^5$ cm^{-2}) emitter. A 3 nm AlN tunneling layer was grown top by plasma-assisted molecular beam epitaxy (details of the growth method are in the Supporting Information). The use of a low TDD density substrate ensures a high film quality and minimal leakage current through the dislocations. A 3 nm GaN layer was used as a capping layer between the AlN and the graphene base.

The surface of the as-grown heterostructure was pinhole free and shows atomic steps with a surface roughness of less than 0.5 nm (the atomic force microscopy image is in the Supporting Information). Electron-beam evaporation was used to deposit an Al film on the back-side to contact the 2-DEG at the AlN/GaN interface through heavily doped n-GaN. To prevent the parasitic conduction between the base and emitter, plasma-enhanced chemical vapor deposition (PECVD) deposited thick SiO_2 was used as isolation dielectric (See Figure 2a). A monolayer graphene thin film was grown by low-pressure chemical vapor deposition (LPCVD) and then transferred with ethyl-vinyl acetate (EVA) as the supporting polymer. [The details of the fabrication method are in the Supporting Information.] The use of EVA ensured that the graphene surface had minimal residue from the transfer process.[34] The transport characteristics of a representative GaN/AlN/graphene diode are shown in Figure 2b. The best performing diode shows a current density of ~10 A/cm^2 at V_{BE} = 2 V, which is ~150× higher than the highest reported current value for oxide tunnel barriers at the same bias.[27] (See Supporting Information for performance comparison of the GaN/AlN B-E barrier with an Al_2O_3 barrier.) The current density can be further increased by using a thinner barrier with improved film quality. The transport through a tunnel barrier can arise from several potential mechanisms, such as direct tunneling of cold electrons through the barrier, Poole−Frenkel emission through the trap states or Fowler−Nordheim tunneling.[27] However, both direct tunneling and Poole−Frenkel emission exhibit a very small selectivity for hot electron generation over that for a cold electron, because carrier transport can occur at any energy in the range from the emitter conduction band to the top of the tunnel barrier. However, the Fowler−Nordheim tunneling mechanism is highly selective for generating hot electrons at the base.[27] According to the Fowler−Nordheim model the current−voltage has the following relationship

$$J \propto E^2 \exp\left(\frac{-K}{E}\right)$$

where K is a constant dependent on the material parameters, E is the electric field across the barrier, and J is the current density. If we plot the diode characteristics as $\log(I/V^2)$ versus V (Figure 2b (inset)), a good fit is achieved with the Fowler−Nordheim tunneling model at higher V_{BE}, which confirms that the dominant transport mechanism is Fowler−Nordheim tunneling at that bias range and is favorable for hot electron generation. Obviously, the thickness of the B−C barrier is crucial for enhancing the injection ratio of the hot electron carriers from the emitter to the collector and minimizing the background B−C cold current emission.

To evaluate the impact of the WSe_2 thickness in our HETs, we fabricated two sets of devices. Device-A is few layer ($N = 4$) WSe_2 barrier and device B is 10 nm thick WSe_2 ($N \sim 16$).

Figure 2c plots the transport characteristics of the B-C diode in device A. The heterojunction was formed by pickup and dry transfer (see the Supporting Information for details) of mechanically exfoliated 4-layer WSe_2 flakes on a prefabricated B-E stack. The diode characteristics showed a weak rectification with a forward to reverse current ratio of 3 at $|V_{BC}| = 1$ V.

Figure 3a shows the common-base GHET characteristics under different emitter injection currents. The emitter current values were selected considering the current levels obtained in

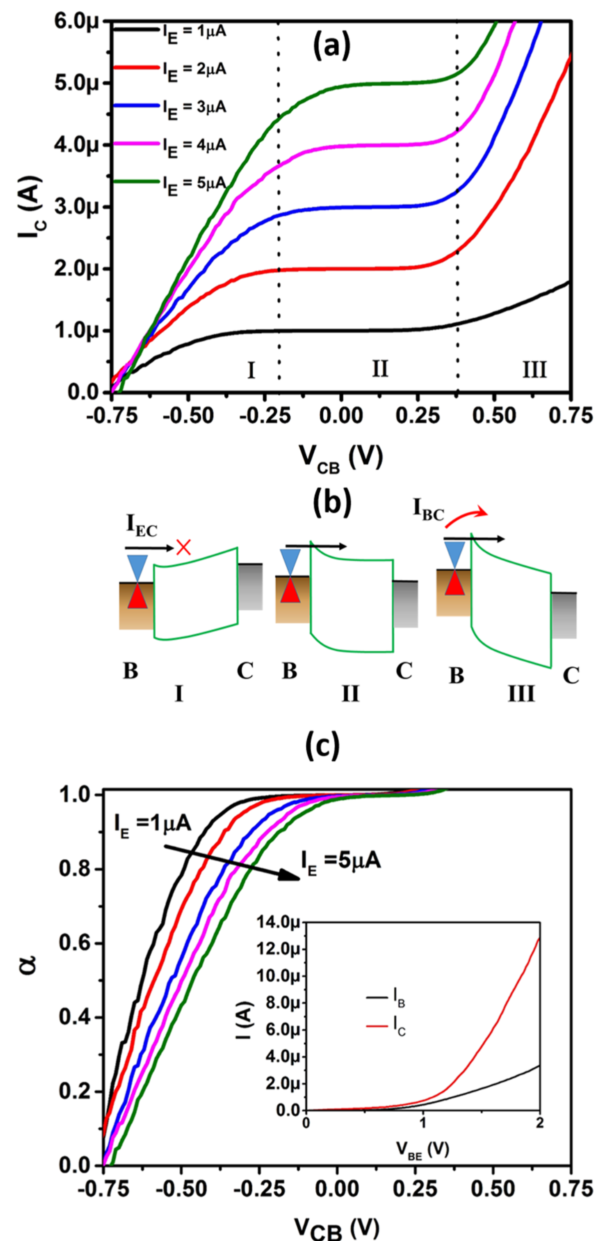

Figure 3. (a) Common-base characteristics of the device A and (b) corresponding schematic energy band diagrams in different operating regions. (c) Injection ratio for device A for different emitter injection currents. Inset shows the Gummel plot for V_{CB} = 0 V.

DOI: 10.1021/acs.nanolett.7b00451
Nano Lett. 2017, 17, 3089−3096

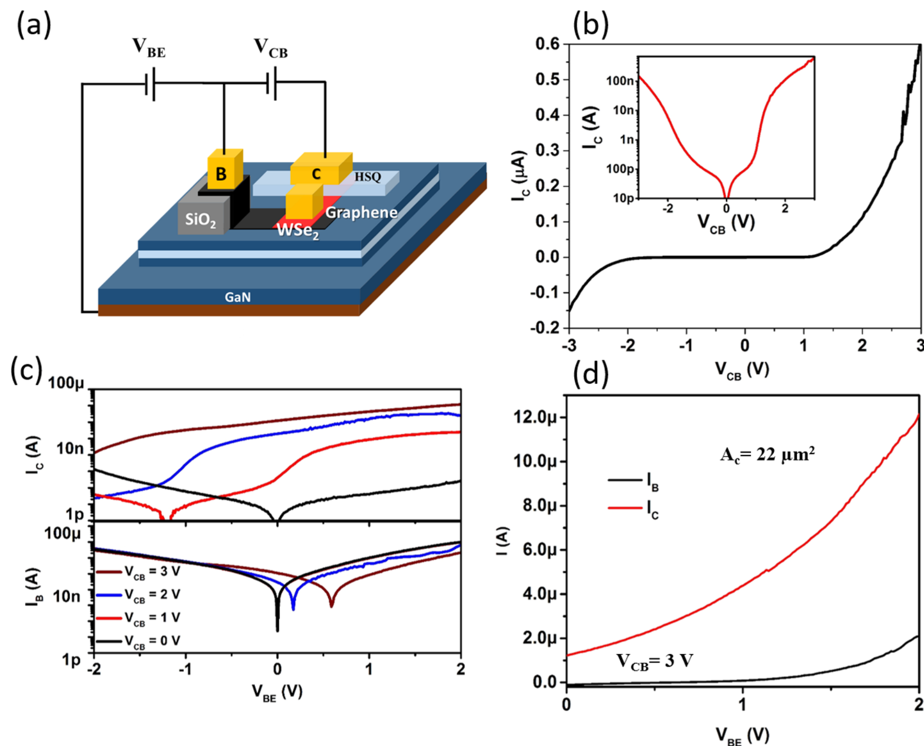

Figure 4. (a) Biasing configuration for electrical characterization of a typical HET. (b) $I-V$ characteristics of the base-collector diode of device B. Inset shows the same plot on a logarithmic scale. (c) I_C, I_B versus V_{BE} characteristics at different V_{CB} values. (d) Gummel plot in the common-emitter configuration for V_{CB} = 3 V.

the B-E diode measurements shown in Figure 2b. In this configuration, the collector bias was swept while the base was grounded. For negative V_{CB} values in region I (forward bias condition of B-C diode), the injected electrons from the emitter encounter the elevated B-C potential barrier as shown in Figure 3b. As a result, the majority of the electrons contribute to the base current after being reflected by the barrier. Maximum reflection occurs at $V_{CB} \sim -0.75$ V, corresponding to the $I_C = 0$ ($I_B = I_E$) condition. However, if V_{CB} is gradually increased toward the reverse bias condition of B-C diode (I → II), the potential barrier decreases and gradually becomes energetically favorable for the injected electrons to surmount the barrier. This effect is evident in Figure 3a, where the collector current increases from zero to the emitter current level owing to the decreased width of the base collector barrier. Figure 3c plots α at this bias range, which increases from zero to approximately unity. However, if we further increase V_{CB} (region III, as shown schematically in Figure 3b), the cold electron leakage increases and becomes the dominating component in I_C, which explains the upturn in current starting at V_{BC} of approximately 0.3 V.

Although this device shows excellent HET characteristics in terms of α, it has a very limited operating V_{BC} window, which suffers from a poor blocking capability of the B−C junction with an ultrathin WSe_2 barrier. This limitation arises from the fact that the WSe_2 flake used in this device is only 4 atomic layers thick, which allows the hot electron to reach the collector with minimum loss but also, as a blocking barrier, works only for a small bias range (region I and II) with a maximum $V_{CB} \sim$ 0.3 V. Increasing the number of layers can improve the blocking as the larger interlayer resistance between layers of WSe_2[35] would suppress the cold electron transport between base and collector. Therefore, to achieve a better blocking capability, further optimization of the barrier geometry is required.

To understand the effect of the barrier thickness, we increased the WSe_2 thickness to 10 nm in device B. The B−C diode characteristics showed that the current through the graphene/WSe_2 diode was much smaller (0.5 nA at V_{CB} = 1 V compared with 200 nA in device A) owing to the increased tunneling resistance.

To characterize the transistor operation, we first biased the device in the common-base mode. Figure 4c plots the base and collector current versus base-emitter voltage at different V_{CB} values. In the absence of an electric field across the B-C junction (V_{CB} = 0 V), the current flow through collector terminal is due to injected carriers from emitter and the current value becomes negligible at V_{BE} = 0 V. If V_{CB} was increased to higher values, the current magnitude at V_{BE} = 2 V shows very small change which indicates that collector current is mainly due to hot electron injection from emitter. However, for lower V_{BE} values we notice a significant increase in the collector current indicating the influence of cold electron leakage (I_{BC}) under these biasing conditions.

Next, we biased the device in the common-emitter configuration to study the gain characteristics. Analogous to BJT, the dc current gain (β) in the HET is defined by the following equation in the common-emitter mode

$$\beta = \frac{I_C}{I_B}$$

For technological applications, it is important to have the current gain at high current values. Figure 4d plots the simultaneous I_C and I_B at V_{CB} = 3 V, where the current value is a maximum and we have gain larger than 1. The resultant current gain at V_{CB} = 3 V was found to be ~5.5 at I_C = 11 μA

DOI: 10.1021/acs.nanolett.7b00451
Nano Lett. 2017, 17, 3089−3096

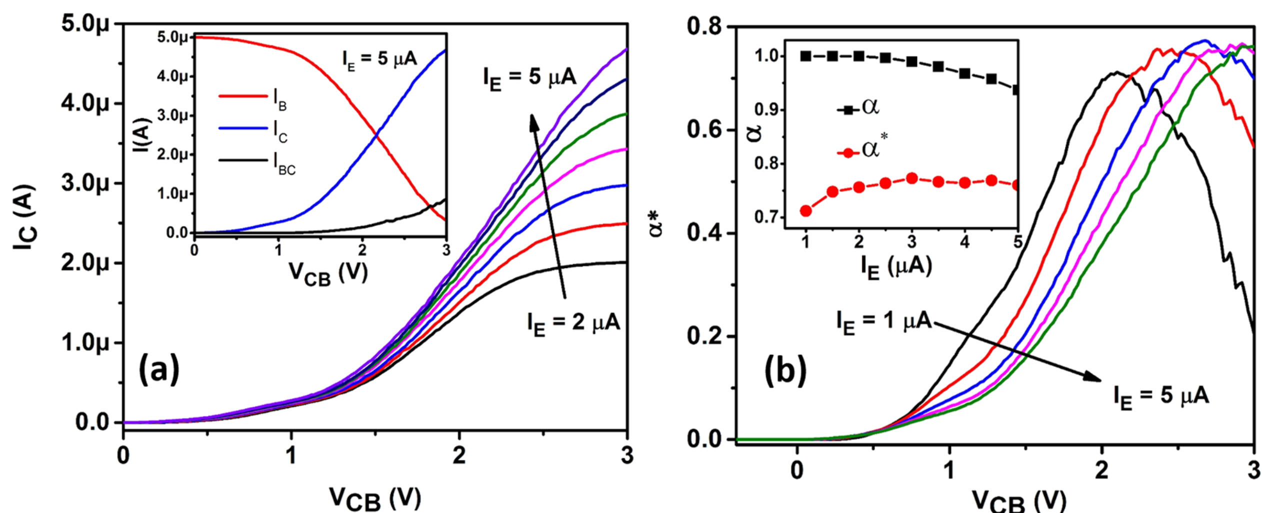

Figure 5. (a) Common-base HET characteristics of the HET at different constant emitter injection currents. The inset compares I_{BC} (the leakage current measured in the two-terminal configuration), I_C and I_B at I_E = 5 μA. (b) Modified injection efficiency in the common-base mode for the characteristics in (a). The inset shows a comparison of the injection efficiencies before and after base-collector cold electron leakage correction as a function of I_E.

(J_C = 50 A/cm^2), which is a record among all graphene-base HETs reported in the literature.

To understand the origin of the current gain, we characterized the device in the common-base configuration with the emitter terminal used as the constant current source. Since the emitter current value was set to a constant value here, the CB mode measurement could evaluate the hot electron filtering capability of the B-C barrier independent of the B-E heterojunction characteristics. At the low bias regime (V_{CB} < 0.7 V), the collector current was negligible, irrespective of the emitter injection current value. This lower collector current value indicated that all the injected electrons from the emitter get reflected at the B-C interface, and eventually thermalize by scattering at the base where they contribute to the base leakage current. At a higher V_{CB}, the energy barrier of the B−C diode becomes thinner and thus allows the hot electron to pass through the barrier. As a result, the collector current increased monotonically until it reached the emitter current. The inset of Figure 5a compares the base and collector currents at I_E = 5 μA and shows a monotonic increase (decrease) of the collector (base) current, which supports the above explanation of the device behavior. Additionally, we should note that using a thicker WSe_2 layer in device B allows a larger V_{CB} voltage up to 3 V, compared with 0.3 V in device A. However, increasing the thickness of WSe_2 would affect the emission rate of the injected hot electrons as they would have to travel a longer physical path from base to the collector.

The emission rate of the injected hot electrons can be quantitatively evaluated by calculating the common-base injection ratio (α), which represents the ratio of electrons successfully transferred to the collector over the total number of injected electrons from the emitter. Because the emitter current is fixed at a constant value in the CB measurement configuration, the trend of the collector current should represent the value of α which reached to 1 at higher V_{CB}. A unity value of α means all the hot electrons injected from the emitter are being transferred to the collector without being lost in the base owing to scattering or reflection at the C-B barrier (i.e., $I_C = I_{EC}$ and I_{BC}= 0). However, at nonzero V_{CB} values, there is a finite current (I_{BC}) flowing between the base and the collector that increases with V_{CB}. The carriers injected from the base to collector are cold electrons, which do not contribute to the amplification. Therefore, calculating α without correcting for B-C leakage overestimates the current gain of the device. Hence, to evaluate the actual amplification potential of the device we define the ballistic injection efficiency α^* to estimate the ratio of electrons quasi-ballistically transferred from the emitter to collector over the total number of injected carriers. To estimate the ballisticity of the device, we subtracted the B-C leakage of the device corresponding to I_E = 0 A from the collector current obtained at nonzero emitter current levels and we define the ballistic injection ratio as $\alpha^* = (I_C - I_C(I_E = 0\ \text{A}))/I_E$.[6] Figure 5b shows α^* for the same biasing conditions used in Figure 5a. At low V_{CB}, α and α^* are essentially the same because the base-collector leakage is negligible. At high V_{CB} biases, the relative increase of α and α^* is different owing to the increase of cold electron injection from the base. The ballistic injection efficiency of the present device is a competition between the hot electron transfer and the efficiency from the emitter and the cold electron injection from the base. As a result, α^* keeps increasing with V_{CB} until it reaches a peak value where the base collector leakage component starts to dominate the collector current and α^* starts to decrease while α keeps increasing. The maximum value of α^* is independent of the injection emitter current level of the emitter, as shown in the inset of Figure 5b. The maximum value of 0.75 indicates that 75% of the injected electrons from the emitter quasi-ballistically travel to the collector terminal, while 25% of the electrons are lost in the base because of reflection. We noted in device A with ultrathin WSe_2, α was approximately 100% with the price of a very low operation V_{CB}. We can calculate the current gain (β) in device B using the following formula, similar to the heterojunction bipolar transistor, $\beta = \alpha/(1 - \alpha)$. The maximum β is found to be ~3, which is consistent with the common-emitter mode β obtained in Figure 3. As the comparison of devices A and B shows, the selection of the collector barrier thickness is a trade-off between the tunneling current density and filtering capability of the barrier. Further in-depth studies based of the targeted device application are required to fully optimize the B-C barrier thickness. Addition-

DOI: 10.1021/acs.nanolett.7b00451
Nano Lett. 2017, 17, 3089−3096

Table 1. Benchmarking of Different Experimental HET Performances

	emitter	base (thickness)	collector barrier	J_C(/cm^2)	β	α
UCSB'15[12]	GaN/AlN	GaN/InGaN (7 nm)	GaN	2.5 kA	>1	>0.5
OSU'16[11]	GaN/AlN	GaN (8 nm)	AlGaN/GaN	46 kA	14.5	0.93
UCLA'15[36]	Si/SiO_2	MoS_2 (0.7 nm)	HfO_2	∼1 μA	4	0.95
KTH'13[25]	Si/SiO_2	graphene (0.4 nm)	Al_2O_3	∼10 μA	0.065	0.065
UCLA'13[24]	Si/SiO_2	graphene (0.4 nm)	Al_2O_3, HfO_2, or Si	∼50 μA	∼0.78	0.44
KTH'15[27]	Si/TmSiO/TiO_2	graphene (0.4 nm)	Si	4 A	0.4	∼0.28
this work	GaN/AlN	graphene (0.4 nm)	WSe_2	∼50 A	4−6	0.75

ally, different layered semiconductors can be studied and benchmarked.

We compare the collector current density and dc current gain of different HETs with sub-10 nm base thickness reported in the literature in Table 1. It is evident that the use of a graphene/semiconductor junction improves J_C, α, and β when compared with the graphene-base oxide collector HETs. (Supporting Information S5 compares the performance of a graphene/WSe_2/Au diode with its counterpart having Al_2O_3 as the barrier.) However, the injection efficiency is still 75% owing to leakage of cold electrons from the base to the collector at the operating condition. A possible solution to enhance the injection efficiency could be the insertion of an ultrathin insulating hBN tunnel barrier between the graphene and WSe_2. The height of the tunnel barrier may prevent the transport of cold electrons near the base conduction band to the collector, while the ultrathin barrier thickness will add minimal resistance to the energetic hot electrons in the base.

In conclusion, we have demonstrated a graphene-base HET with record performance by using a graphene/WSe_2 heterojunction as a base-collector barrier on GaN. This hybrid GaN/vdW HET exhibits J_C of 50 A/cm^2, β in excess of 3, and α^* of 0.75, which can be further improved by a structural and geometric optimization of the device structure. To the best of our knowledge, this work is the first demonstration of the integration of GaN and a van der Waals heterostructure in HETs and is hoped to lead the way for numerous novel device structures that can be implemented by integrating these two unique material systems.

ASSOCIATED CONTENT

Supporting Information

The Supporting Information is available free of charge on the ACS Publications website at DOI: 10.1021/acs.nanolett.7b00451.

Additional data concerning the AlN growth, device fabrication, graphene growth and transfer, heterostructure fabrication by dry transfer technique, and electrical characterization of HET with high-κ dielectric barriers (PDF)

AUTHOR INFORMATION

Corresponding Author

*E-mail: azubair@mit.edu.

ORCID

Ahmad Zubair: 0000-0001-9827-3557

Meng Qi: 0000-0002-9943-0056

Notes

The authors declare no competing financial interest.

ACKNOWLEDGMENTS

The authors would like to thank Redwan N. Sajjad, Min Sun for helpful discussions on this work, and Professor Pablo-Jarillo Herrero for providing research facilities. This work has been partially supported by the ARO Grant W911NF-14-2-0071 (monitored by Dr. Joe Qiu), ONR PECASE program, the STC Center for Integrated Quantum Materials, NSF Grant DMR-1231319, and the AFOSR FATE MURI, Grant FA9550-15-1-0514.

REFERENCES

(1) Mead, C. A. *J. Appl. Phys.* **1961**, *32* (4), 646−652.
(2) Muratake, S.; Watanabe, M.; Suemasu, T.; Asada, M. *Electron. Lett.* **1992**, *28* (11), 1002−1004.
(3) Heiblum, M.; Thomas, D. C.; Knoedler, C. M.; Nathan, M. I. *Appl. Phys. Lett.* **1985**, *47* (10), 1105.
(4) Levi, A. F. J.; Chiu, T. H. *Appl. Phys. Lett.* **1987**, *51* (13), 984−986.
(5) Yokoyama, N.; Imamura, K.; Ohnishi, H.; Mori, T.; Muto, S.; Shibatomi, A. *Solid-State Electron.* **1988**, *31* (3−4), 577−582.
(6) Moise, T. S.; Seabaugh, A. C.; Beam, E. A.; Randall, J. N. *IEEE Electron Device Lett.* **1993**, *14* (9), 441−443.
(7) Yajima, T.; Hikita, Y.; Hwang, H. Y. *Nat. Mater.* **2011**, *10* (3), 198−201.
(8) Tonouchi, M.; Sakai, H.; Kobayashi, T.; Fujisawa, K. *IEEE Trans. Magn.* **1987**, *23* (2), 1674−1677.
(9) Dasgupta, S.; Raman, A.; Speck, J. S.; Mishra, U. K. *IEEE Electron Device Lett.* **2011**, *32* (9), 1212−1214.
(10) Shur, M. S.; Bykhovski, A. D.; Gaska, R.; Khan, M. A.; Yang, J. W. *Appl. Phys. Lett.* **2000**, *76* (22), 3298−3300.
(11) Yang, Z. C.; Zhang, Y. W.; Krishnamoorthy, S.; Nath, D. N.; Khurgin, J. B.; Rajan, S. *Appl. Phys. Lett.* **2016**, *108* (19), 192101.
(12) Gupta, G.; Ahmadi, E.; Hestroffer, K.; Acuna, E.; Mishra, U. K. *IEEE Electron Device Lett.* **2015**, *36* (5), 439−441.
(13) Novoselov, K. S.; Mishchenko, A.; Carvalho, A.; Castro Neto, A. H. *Science* **2016**, *353* (6298), aac9439.
(14) Britnell, L.; Gorbachev, R. V.; Jalil, R.; Belle, B. D.; Schedin, F.; Mishchenko, A.; Georgiou, T.; Katsnelson, M. I.; Eaves, L.; Morozov, S. V.; Peres, N. M. R.; Leist, J.; Geim, A. K.; Novoselov, K. S.; Ponomarenko, L. A. *Science* **2012**, *335* (6071), 947−950.
(15) Yang, H.; Heo, J.; Park, S.; Song, H. J.; Seo, D. H.; Byun, K. E.; Kim, P.; Yoo, I.; Chung, H. J.; Kim, K. *Science* **2012**, *336* (6085), 1140−1143.
(16) Mishchenko, A.; Tu, J. S.; Cao, Y.; Gorbachev, R. V.; Wallbank, J. R.; Greenaway, M. T.; Morozov, V. E.; Morozov, S. V.; Zhu, M. J.; Wong, S. L.; Withers, F.; Woods, C. R.; Kim, Y. J.; Watanabe, K.; Taniguchi, T.; Vdovin, E. E.; Makarovsky, O.; Fromhold, T. M.; Fal'ko, V. I.; Geim, A. K.; Eaves, L.; Novoselov, K. S. *Nat. Nanotechnol.* **2014**, *9* (10), 808−813.
(17) Kong, B. D.; Jin, Z.; Kim, K. W. *Phys. Rev. Appl.* **2014**, *2* (5), 054006.
(18) Di Lecce, V.; Grassi, R.; Gnudi, A.; Gnani, E.; Reggiani, S.; Baccarani, G. *IEEE Trans. Electron Devices* **2013**, *60* (12), 4263−4268.
(19) Venica, S.; Driussi, F.; Palestri, P.; Esseni, D.; Vaziri, S.; Selmi, L. *IEEE Trans. Electron Devices* **2014**, *61* (7), 2570−2576.

(20) Driussi, F.; Palestri, P.; Selmi, L. *Microelectron. Eng.* **2013**, *109*, 338−341.
(21) Mehr, W.; Dabrowski, J.; Scheytt, J. C.; Lippert, G.; Xie, Y. H.; Lemme, M. C.; Ostling, M.; Lupina, G. *IEEE Electron Device Lett.* **2012**, *33* (5), 691−693.
(22) Di Lecce, V.; Grassi, R.; Gnudi, A.; Gnani, E.; Reggiani, S.; Baccarani, G. *IEEE Trans. Electron Devices* **2013**, *60* (10), 3584−3591.
(23) Venica, S.; Driussi, F.; Palestri, P.; Selmi, L. *Microelectron. Eng.* **2015**, *147*, 192−195.
(24) Zeng, C.; Song, E. B.; Wang, M.; Lee, S.; Torres, C. M., Jr.; Tang, J.; Weiller, B. H.; Wang, K. L. *Nano Lett.* **2013**, *13* (6), 2370−5.
(25) Vaziri, S.; Lupina, G.; Henkel, C.; Smith, A. D.; Ostling, M.; Dabrowski, J.; Lippert, G.; Mehr, W.; Lemme, M. C. *Nano Lett.* **2013**, *13* (4), 1435−9.
(26) Vaziri, S.; Smith, A. D.; Ostling, M.; Lupina, G.; Dabrowski, J.; Lippert, G.; Mehr, W.; Driussi, F.; Venica, S.; Di Lecce, V.; Gnudi, A.; Konig, M.; Ruhl, G.; Belete, M.; Lemme, M. C. *Solid State Commun.* **2015**, *224*, 64−75.
(27) Vaziri, S.; Belete, M.; Dentoni Litta, E.; Smith, A. D.; Lupina, G.; Lemme, M. C.; Ostling, M. *Nanoscale* **2015**, *7* (30), 13096−104.
(28) Nath, D. N.; Yang, Z. C.; Lee, C. Y.; Park, P. S.; Wu, Y. R.; Rajan, S. *Appl. Phys. Lett.* **2013**, *103* (2), 022102.
(29) Suntrup, D. J.; Gupta, G.; Li, H. R.; Keller, S.; Mishra, U. K. *Appl. Phys. Lett.* **2014**, *105*, 26.
(30) Nourbakhsh, A.; Adelmann, C.; Song, Y.; Lee, C. S.; Asselberghs, I.; Huyghebaert, C.; Brizzi, S.; Tallarida, M.; Schmeisser, D.; Van Elshocht, S.; Heyns, M.; Kong, J.; Palacios, T.; De Gendt, S. *Nanoscale* **2015**, *7* (24), 10781−10789.
(31) Lan, Y. W.; Torres, C. M., Jr.; Zhu, X.; Qasem, H.; Adleman, J. R.; Lerner, M. B.; Tsai, S. H.; Shi, Y.; Li, L. J.; Yeh, W. K.; Wang, K. L. *Sci. Rep.* **2016**, *6*, 32503.
(32) Tongay, S.; Lemaitre, M.; Schumann, T.; Berke, K.; Appleton, B. R.; Gila, B.; Hebard, A. F. *Appl. Phys. Lett.* **2011**, *99* (10), 102102.
(33) Kim, K.; Larentis, S.; Fallahazad, B.; Lee, K.; Xue, J. M.; Dillen, D. C.; Corbet, C. M.; Tutuc, E. *ACS Nano* **2015**, *9* (4), 4527−4532.
(34) Hong, J. Y.; Shin, Y. C.; Zubair, A.; Mao, Y.; Palacios, T.; Dresselhaus, M. S.; Kim, S. H.; Kong, J. *Adv. Mater.* **2016**, *28* (12), 2382−92.
(35) Das, S.; Appenzeller, J. *Phys. Status Solidi RRL* **2013**, *7* (4), 268−273.
(36) Torres, C. M., Jr.; Lan, Y. W.; Zeng, C.; Chen, J. H.; Kou, X.; Navabi, A.; Tang, J.; Montazeri, M.; Adleman, J. R.; Lerner, M. B.; Zhong, Y. L.; Li, L. J.; Chen, C. D.; Wang, K. L. *Nano Lett.* **2015**, *15* (12), 7905−12.

DOI: 10.1021/acs.nanolett.7b00451
Nano Lett. 2017, 17, 3089−3096